

Deep learning enables ultraviolet photoacoustic microscopy based histological imaging with near real-time virtual staining

Lei Kang, Xiufeng Li, Yan Zhang, Terence T.W. Wong ^{*}

Translational and Advanced Bioimaging Laboratory, Department of Chemical and Biological Engineering, The Hong Kong University of Science and Technology, Kowloon, Hong Kong, China

ARTICLE INFO

Keywords:

Deep learning
Unsupervised learning
Photoacoustic microscopy
Histological imaging

ABSTRACT

Histological images can reveal rich cellular information of tissue sections, which are widely used by pathologists in disease diagnosis. However, the gold standard for histopathological examination is based on thin sections on slides, which involves inevitable time-consuming and labor-intensive tissue processing steps, hindering the possibility of intraoperative pathological assessment of the precious patient specimens. Here, by incorporating ultraviolet photoacoustic microscopy (UV-PAM) with deep learning, we show a rapid and label-free histological imaging method that can generate virtually stained histological images (termed Deep-PAM) for both thin sections and thick fresh tissue specimens. With the tissue non-destructive nature of UV-PAM, the imaged intact specimens can be reused for other ancillary tests. We demonstrated Deep-PAM on various tissue preparation protocols, including formalin-fixation and paraffin-embedding sections (7- μm thick) and frozen sections (7- μm thick) in traditional histology, and rapid assessment of intact fresh tissue ($\sim 2\text{-mm}$ thick, within 15 min for a tissue with a surface area of 5 mm \times 5 mm). Deep-PAM potentially serves as a comprehensive histological imaging method that can be simultaneously applied in preoperative, intraoperative, and postoperative disease diagnosis.

1. Introduction

Histopathology is a histology branch that includes detailed microscopic observations and study of diseased tissues [1], which plays a significant role in accurate cancer diagnosis and identification of diseases as histological images provide rich information about the tissue sections, such as the cell distribution and cellular components [2]. In conventional histology, formalin-fixation and paraffin-embedding (FFPE) is the most commonly used method as the resulting histological images are with high quality, and it allows permanent tissue preservation. However, the sample preparation procedure involves a series of laborious and costly procedures, including FFPE, high-quality sectioning (typically 2–7 μm), specimen mounting, and subsequent histological staining, causing a delay of the generation of histological images ranging from days to weeks [3] (Fig. 1), hence, limiting its application to only pre or post-operative situations. To simplify the sample preparation procedures, deep-learning-based virtual staining methods [4,5] have been applied to substitute the histological staining step, eliminating the time and chemical cost needed for staining. However, most of the previously reported virtual staining neural networks have to be trained on unstained and stained histological image pairs,

which are difficult to acquire and require a complicated image registration process before feeding into the networks. Moreover, compared with the total time of histological sample preparation (days), the staining time accounts for a relatively minor part only (minutes to hours), while most times are spent on tissue processing for high-quality sectioning. Consequently, conventional histology incorporated with deep-learning virtual staining still requires several days to obtain histological images, hindering its usage in time-sensitive clinical applications, such as intraoperative diagnosis.

Frozen section offers a rapid alternative to FFPE histology by freezing the tissue before sectioning, which takes around 20–30 min for preparation and turnaround time [6], allowing intraoperative diagnosis for breast-conserving surgery (BCS) [7] and surgical management of brain tumors [8]. However, the fundamental limitations of frozen section create hurdles to use it in more applications, e.g., inherent freezing artifacts, especially when dealing with lipid-rich tissues [9]. The crystal formed in the tissue can cause a false sense of a minimal increase in cellularity [10], leading to misinterpretations and diagnostic pitfalls.

Given the limitations of frozen section and FFPE section, novel imaging approaches have been developed to acquire histological images of unsectioned fresh tissue directly. According to the imaging modalities'

* Corresponding author.

E-mail addresses: lkangaa@connect.ust.hk (L. Kang), xlies@connect.ust.hk (X. Li), yzhangid@connect.ust.hk (Y. Zhang), ttwwong@ust.hk (T.T.W. Wong).

contrast, these methods can be divided into (i) label-free methods using endogenous contrasts provided by the intrinsic biomolecules, and (ii) labeling methods relying on the exogenous contrast agents such as fluorescent dyes. Taking the advantage of fluorescent dyes, confocal microscopy [11,12], nonlinear (two photon [13] and second harmonic [14]) microscopy, structure illumination microscopy (SIM) [15], microscopy with ultraviolet surface excitation (MUSE) [16,17] and light-sheet microscopy [18] have been proven as powerful techniques to acquire molecular-specific images of unsectioned fresh tissue. Subsequently, a model-based pixel value mapping can produce pseudo histological images from fluorescence signals to hematoxylin and eosin (H&E) staining [19]. Among these imaging methods, confocal and nonlinear microscopy can provide superior image resolution and contrast, as they only detect fluorescence signals emitted from the tightly focused focal volume. SIM, MUSE, and light-sheet microscopy are alternative methods that employ wide-field illumination, improving the imaging speed significantly. SIM relies on the defined spatial illumination pattern to provide optical sectioning ability while MUSE relies on the limited penetration depth of ultraviolet (UV) light. The sectioning ability of light-sheet microscopy comes from the decoupling of the illumination light sheet and the detection optics [20]. The unique decoupled optical setup in light-sheet microscopy also minimizes the effect of the photo-bleaching, a common disadvantage of fluorescence microscopy. However, the photo-bleaching effect is still inevitable in the focal plane. Consequently, although fluorescence imaging is powerful for providing information on the morphology of different biomolecules in cells, the photo-toxicity to cells and the photo-bleaching problems will downgrade the image quality. Moreover, exogenous labels may interfere with cell metabolism and adversely affect subsequent clinical implementations. It is also worth noting that the fluorescence dyes are

potentially toxic [21] and may cause potential side effects, which could impede their use in operating rooms.

Given this, label-free imaging modality is highly desirable in modern clinical settings. Stimulated Raman scattering (SRS) [22] and coherent anti-Stokes Raman scattering [23], where image features are characterized by intrinsic molecular vibration, have been proven as a label-free imaging modality for unsectioned fresh tissue. Moreover, non-linear processes originated from a non-centrosymmetric interface, including second-harmonic generation [24], third-harmonic generation [25], and their compound modalities (SLAM) [26] have demonstrated their capability to visualize various cellular components. However, a high-power ultrafast laser is essential to implement these imaging methods to sustain high detection sensitivity and provide high molecular contrast, which is not readily available in most clinical settings. Besides, reflectance-based methods such as optical coherence tomography have been successfully applied in clinical trials for label-free imaging of human breast tissue [27]. However, it is not designed to acquire images at subcellular resolution as required in standard-of-care clinical histopathology.

Ultraviolet photoacoustic microscopy (UV-PAM) is a label-free imaging modality that can generate histological images of biological tissue surface without physical sectioning [28]. By the intrinsic optical absorption contrast, UV laser illumination has the advantage of highlighting cell nuclei with cytoplasm serving as the background, thus providing a similar contrast as H&E labeling used in conventional histology [29]. Unlike nonlinear microscopy, UV-PAM is not demanding in the system configuration while providing subcellular resolution. Recently, our group has developed a galvanometer mirror-based UV-PAM (GM-UV-PAM) system to further improve the imaging speed, thus, promoting its applications in intraoperative surgical margin

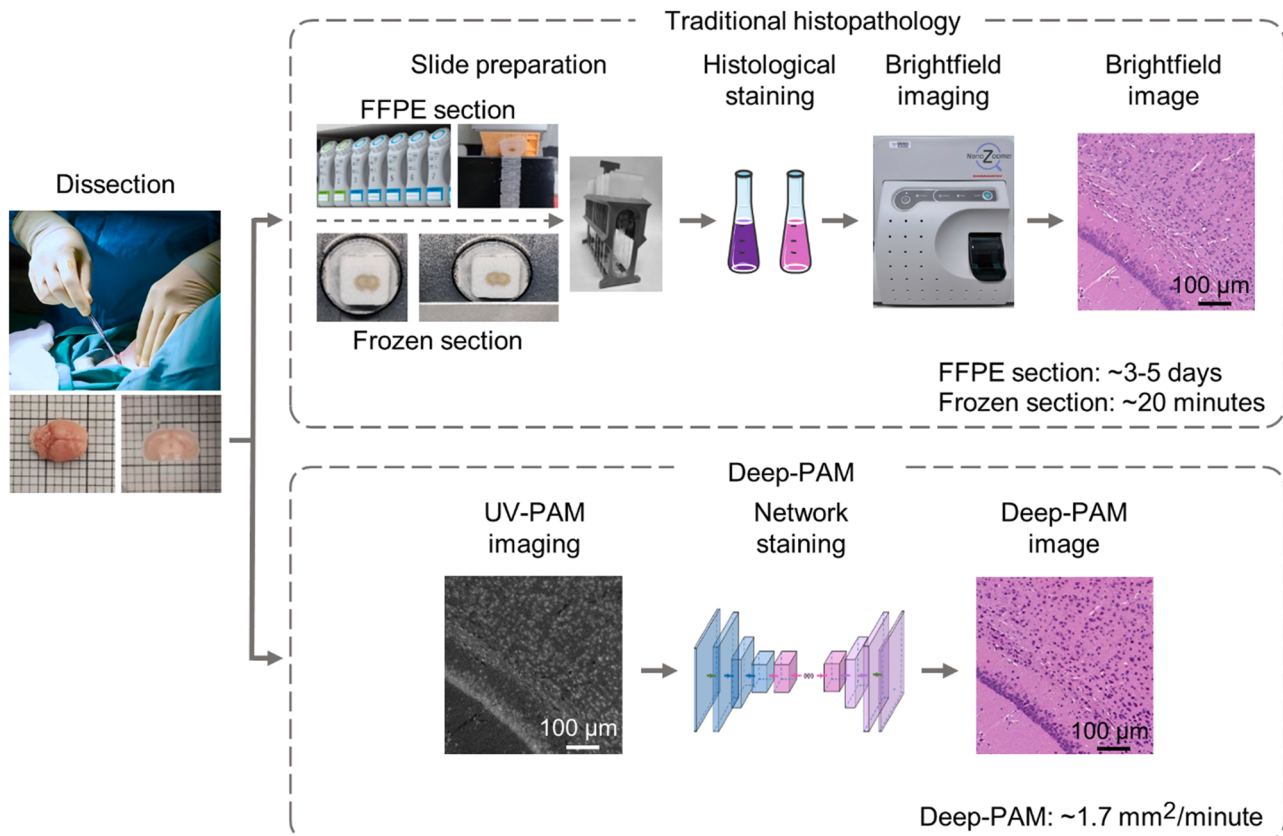


Fig. 1. Illustration of the workflow to obtain histological images in traditional histopathology and Deep-PAM. Biological tissue (e.g., a mouse brain) is harvested and cut by hand. The top pathway shows the two traditional methods to obtain H&E-stained histological images of thin sections from FFPE and frozen section, respectively. The bottom pathway illustrates our proposed method using UV-PAM imaging and deep-learning-based virtual staining that can directly and rapidly get virtual H&E-stained histological images (i.e., Deep-PAM) of fresh thick tissue.

analysis [30].

To build upon the strength of GM-UV-PAM, here, we propose to apply an unpaired image-to-image translation network (e.g., cycle-consistent adversarial network (CycleGAN)) to GM-UV-PAM images, instantly generating H&E equivalent images of unprocessed tissues. Unlike conventional histological methods based on thin slides, which involve slice preparation and chemical staining, our method does not require any sample preparation after tissue excision. GM-UV-PAM is used to image an unprocessed specimen to get histological images. Then, a CycleGAN network is applied to transform the GM-UV-PAM histological images to virtual H&E-stained images (termed Deep-PAM hereafter) that pathologists are familiar with (Fig. 1). In the following, we show that our approach can produce high-quality histological images that are comparable to conventional histological images obtained in traditional histopathology using thin FFPE sections (Fig. 4). Then, we demonstrate that our approach can provide better histological images than that of frozen section using thin frozen tissue sections (Fig. 5). Finally, the ability of GM-UV-PAM to rapidly image a hand-cut fresh thick tissue surface is also demonstrated and verified by providing the FFPE-based histological images of the adjacent layer of the imaged tissue surface (Fig. 6).

The utilization of CycleGAN removes the need for the histological staining process, promisingly providing a simplified alternative for preoperative and postoperative pathological examinations. More importantly, GM-UV-PAM allows high-speed histological imaging of fresh and unsectioned tissue, which eliminates all the sample preparation steps, making Deep-PAM highly favorable for intraoperative diagnosis.

2. Methods

2.1. GM-UV-PAM system

The GM-UV-PAM system (Fig. 2a) acquires UV-PAM images of thin FFPE sections, frozen sections, and thick fresh brain specimens. The entire system is governed by a controller (MyRIO-1900, National Instruments Corp.) that integrates an onboard field-programmable gate array (FPGA) and a Xilinx-Z microprocessor. The controller dispatches three-way synchronized signals through its FPGA pinouts to coordinate the laser, data acquisition card, and scanning system. Once the UV

pulsed laser (266 nm wavelength, WEDGE HF 266 nm, Bright Solution Srl.) receives a trigger from the controller, a laser pulse will be generated, expanded by a pair of plano-convex lenses (LA-4600-UV, LA-4633-UV, Thorlabs Inc.) and then focused on the tissue by an objective lens (LMU-20X-UVB, Thorlabs Inc.), after which the tissue will absorb the energy of the laser pulse and emit PA signals. The PA signals are focused and detected by an ultrasonic transducer (V324-SU, 25 MHz, Olympus NDT Inc.), amplified by amplifiers (56 dB, two ZFL-500LN-BNC+, Mini-circuits Inc.), and recorded by a data acquisition card (ATS9350, Alazar Technologies Inc.). With the help of the scanning system—a single-axis galvo mirror (GVS411, Thorlabs Inc.) and two motorized translation stages (L-509.10SD00, Physik Instruments (PI) GmbH & Co.KG), the PA signals of the whole tissue can be acquired point-by-point with a pixel scanning rate up to 55k (determined by the laser repetition rate). The recorded data will be mapped to a UV-PAM image on the desktop through a customized Labview (National Instruments.) interface.

The deparaffinized brain sections prepared by FFPE sectioning, and the brain sections produced by frozen sectioning, were imaged by the GM-UV-PAM system to obtain their UV-PAM images. After imaging, these brain slices were stained by H&E, and then captured by a bright-field whole sliding imaging machine (Nanoozoomer-SQ C13140, Hamamatsu Photonics K.K.) with a focusing objective lens (20X, NA = 0.75, CFI Plan Apo Lambda 20x) to acquire their corresponding BF-H&E images. For the hand-cut thick and fresh brain specimen, it was directly imaged by the GM-UV-PAM system without any other tissue processing steps. The specimen was then sent for conventional FFPE sample preparation to get the BF-H&E histological image of the layer next to the imaged surface.

2.2. Deep-learning virtual staining

The GM-UV-PAM can produce histological images (i.e., UV-PAM images) that share similar imaging contrast as H&E, while the CycleGAN neural network is able to digitally stain the UV-PAM images to BF-H&E stained images (i.e., Deep-PAM images). We adopted the CycleGAN architecture from Zhu et al. [31] and improve it to fit in our application. The CycleGAN is composed of four deep neural networks, two generators (G, F), and two discriminators (X, Y). The detailed structures of the generator networks and discriminator networks are shown in Supplementary Fig. S1. In Fig. 2b, generator G learns to transform UV-PAM

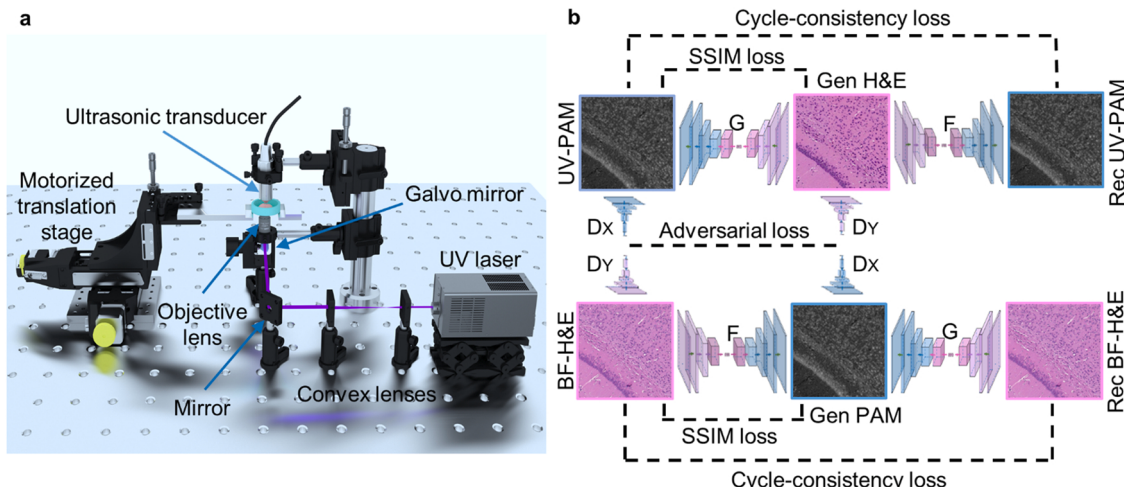


Fig. 2. Illustration of the GM-UV-PAM system and CycleGAN virtual staining framework. a, The schematic of the GM-UV-PAM system that generates high-quality UV-PAM images of biological tissues. b, Detailed workflow of the transformation between UV-PAM and BF-H&E images using CycleGAN architecture. The generator G transforms the UV-PAM to BF-H&E images, while the generator F translates the BF-H&E to UV-PAM images. The SSIM loss is calculated between input and generated images. The discriminator X (D_X) distinguishes the real UV-PAM from the generated UV-PAM images (Gen PAM), whereas the discriminator Y (D_Y) distinguishes the real BF-H&E from the generated BF-H&E images (Gen H&E). The outputs of discriminators are used to calculate the adversarial loss. The generator F also transforms the generated BF-H&E images back to UV-PAM images (Rec UV-PAM), which will be used to compare with the original UV-PAM images to calculate the cycle-consistency loss. The generator G works similarly to the generator F .

images to BF-H&E images, while generator F transforms BF-H&E images back to UV-PAM images. Discriminator X (D_X) aims to distinguish the real UV-PAM images from the generated UV-PAM images produced by the generator F, whereas, discriminator Y (D_Y) aims to distinguish the real BF-H&E images from the generated H&E images produced by the generator G. Once the generator G can produce H&E images that D_Y cannot distinguish from the real BF-H&E images, it means the generator G has learned the transformation from UV-PAM to H&E images. And this is also applicable to generator F and D_X .

In Fig. 2b, after inputting a UV-PAM image to generator G, it will output a generated BF-H&E image. D_Y will determine if this generated BF-H&E image is real or fake, and this generated BF-H&E image goes through the generator F to be transformed back to a UV-PAM image called recovered UV-PAM image. The mean absolute error between the input UV-PAM and recovered UV-PAM images is called cycle-consistency loss. Similarly, begin from the BF-H&E image, generator F learns to transform BF-H&E images to UV-PAM images, D_X will determine if the generated UV-PAM image is real or fake, and the generated UV-PAM image will be transformed back to an H&E image by generator G. Besides, D_X and D_Y will also determine the truthfulness of real BF-H&E and UV-PAM images. These four discriminator losses compose the adversarial loss.

The objective of the original CycleGAN contains three types of losses, adversarial loss [32], cycle-consistency loss [31], and identity loss. Following the original CycleGAN losses, we add structure similarity index measure (SSIM) loss [33] in the objective.

$$\mathcal{L}_{ssim}(G, F) = 1 - E_{x \sim p_{data}(x)}[\text{SSIM}(x, G(x))] + (1 - E_{y \sim p_{data}(y)}[\text{SSIM}(y, F(y))]) \quad (1)$$

Therefore, the improved CycleGAN objective in our application is:

$$\begin{aligned} \mathcal{L}(G, F, D_X, D_Y) &= \mathcal{L}_{GAN}(G, D_Y, X, Y) + \mathcal{L}_{GAN}(F, D_X, Y, X) \\ &\quad + \eta \mathcal{L}_{cyc}(G, F) \\ &\quad + \gamma \mathcal{L}_{identity}(G, F) + \kappa \mathcal{L}_{ssim}(G, F) \end{aligned} \quad (2)$$

where $\eta = 10$, $\gamma = 1$, $\kappa = 2$ in our experiments. The numbers of η , γ are adopted from the original paper of CycleGAN [31]. We choose a κ value that minimizes the SSIM loss.

The SSIM loss imposes restrictions on the transformation between UV-PAM image and the corresponding Deep-PAM image, making sure that the generated detailed features are strictly from the UV-PAM image, not a random structure. Consequently, the CycleGAN model trained with SSIM loss tends to output more authentic and reliable Deep-PAM images, which can be validated in [Supplementary Fig. S2](#).

2.3. Network training and evaluation

In the CycleGAN training experiments, we flipped the amplitude of the UV-PAM images, so the color of nuclei turns black. While training with flipped UV-PAM images, we found that the network training process gets more stable and the generator G can generate desired BF-H&E images with less training time. The flipped UV-PAM image was then cut into small tiles (256×256) by a sliding window with a moving step of 150 pixels. As the magnifications of the UV-PAM image and BF-H&E image were different, the BF-H&E image was first downsampled to map the UV-PAM image and then cropped by the same algorithm. The downsampling ratio is determined by the ratio of measured pixel numbers of the same structure in UV-PAM image and BF-H&E image, which is around 2.2 for our case.

Two CycleGAN neural networks were respectively trained for virtual staining of thin brain sections and a thick fresh brain. As the CycleGAN network can virtually stain both FFPE and frozen thin sections, it was trained on a dataset composed of UV-PAM and BF-H&E images of 7-μm thick FFPE thin sections only. It should be noticed that the UV-PAM

images and BF-H&E images were generated from different FFPE mouse brain sections since we took advantage of the unpaired training superiority of the CycleGAN architecture. As for the CycleGAN network that can digitally stain the thick fresh tissue, it is trained on a dataset composed of UV-PAM and BF-H&E images, where the UV-PAM images were acquired from fresh tissue, and the BF-H&E images were cropped from BF-H&E images of 7-μm thick FFPE brain sections. The training details of these two networks are listed in [Table 1](#).

Even though the generative adversarial loss in the GAN network is not the main indicator of the performance of the training, the cycle-consistency loss is highly reliable as it reflects the networks' ability to recover the original image. [Fig. 3a](#) and b show the cycle-consistency loss of UV-PAM images during different epochs. As the training epoch increases, the loss gradually decreases and finally oscillates around a stable value, showing that the output Deep-PAM images are highly stable and consistent. Hence, this loss indicates that it can be served as a reference to terminate the training.

The network was implemented using Python version 3.7.3, with Pytorch version 1.0.1. The software was implemented on a desktop computer with a Core i7-9700K CPU@3.6 GHz and 64 GB RAM, running an Ubuntu 18.04.2 LTS operation system. The CycleGAN neural networks' training and testing were performed using a NVIDIA Titan RTX GPU with 24 GB RAM.

2.4. Animal organ extraction and tissue processing

The organs were extracted from C57BL/6 mouse. After the euthanasia with the inhalation of carbon dioxide, the mouse brains were harvested immediately. The protocols for the FFPE section and the frozen section are different, and we followed the standard protocols from the IHC World. All experiments were carried out in conformity with a laboratory animal protocol approved by the Health, Safety and Environment Office of The Hong Kong University of Science and Technology.

As for the preparation of FFPE tissue sections, the extracted fresh brain from the mouse was firstly fixed with 10% formalin for 24 h and then undertook a series of operations including dehydration, clearing, and paraffin infiltration within a Revos Tissue Processor (ThermoFisher Scientific Inc.), which take ~ 13 h. Subsequently, the brain was trimmed and embedded into a paraffin block using a HistoStar Embedding Workstation (ThermoFisher Scientific Inc.) before sectioned into 7-μm thin sections by a microtome. These brain sections were mounted on quartz slides followed by a 30-min air drying and 60-min baking in a 60 °C incubator before they were deparaffinized with xylene. The deparaffinized brain slides were preserved in distilled water and ready for GM-UV-PAM imaging or H&E staining.

Following the IHC World's protocol for fixed frozen tissues, the fresh mouse brain was fixed in 10% neutral buffered formalin for 8 h. The fixed brain was immersed with 15% sucrose in phosphate-buffered saline (PBS) until it was sunk and then in 30% sucrose in PBS overnight before embedded in optimal cutting temperature (OCT) compound for freezing. The perfusion of sucrose solution is able to help to reduce the formation of ice crystals that break cell membranes and produce holes within cells during tissue freezing. The OCT embedded brain is cut to 7-μm thin sections by a cryostat—Cryostar NX70 (ThermoFisher Scientific

Table 1

Training details of the CycleGAN networks which can stain thin FFPE sections and the surface of thick and fresh tissue.

Networks	# of patches	# of iterations	# of epochs	Training Time (h)
Staining for thin sections	400	40,000	100	3
Staining for thick and fresh tissue	800	80,000	100	6

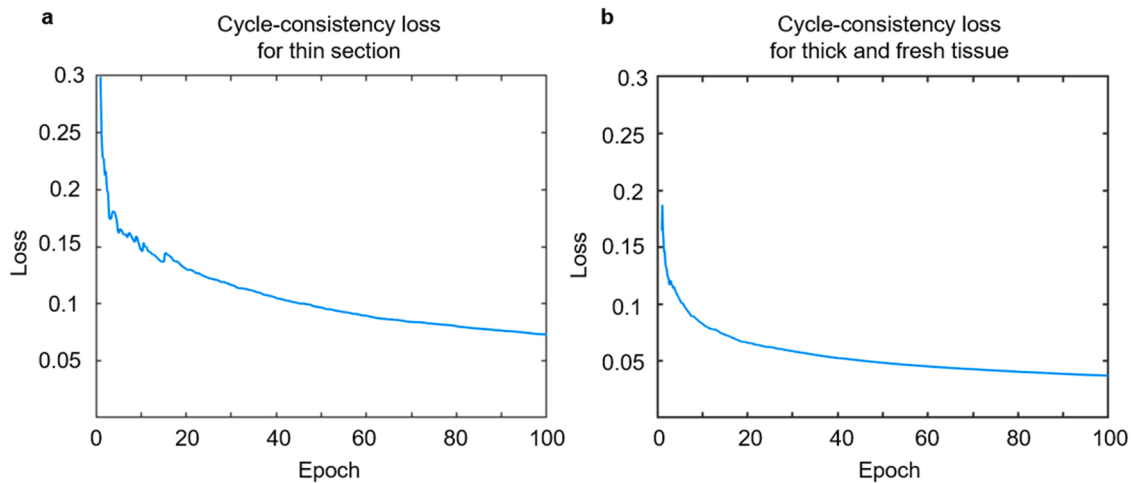


Fig. 3. CycleGAN training losses. a, The cycle-consistency loss of UV-PAM images in the CycleGAN training (for thin section virtual staining). b, The cycle-consistency loss of UV-PAM images in the CycleGAN training (for thick and fresh tissue surface virtual staining).

Inc.). The thin brain sections were mounted on quartz slides and air-dried for 30 min before imaged by UV-PAM or stained by H&E.

As for the preparation of the thick and fresh brain specimen, the dissected fresh brain was first embedded in agarose for immobilization and then cut to 2–4 mm thick blocks by hand. After imaged by the GM-UV-PAM system, the imaged fresh brain specimen went through the FFPE tissue processing procedure mentioned above to cut out the layer

next to the imaged surface. The 7- μm thick layer, which is adjacent to the imaged fresh brain surface, was stained by H&E get the ground truth H&E-stained image.

3. Results

We initially demonstrated the effectiveness of our UV-PAM-based

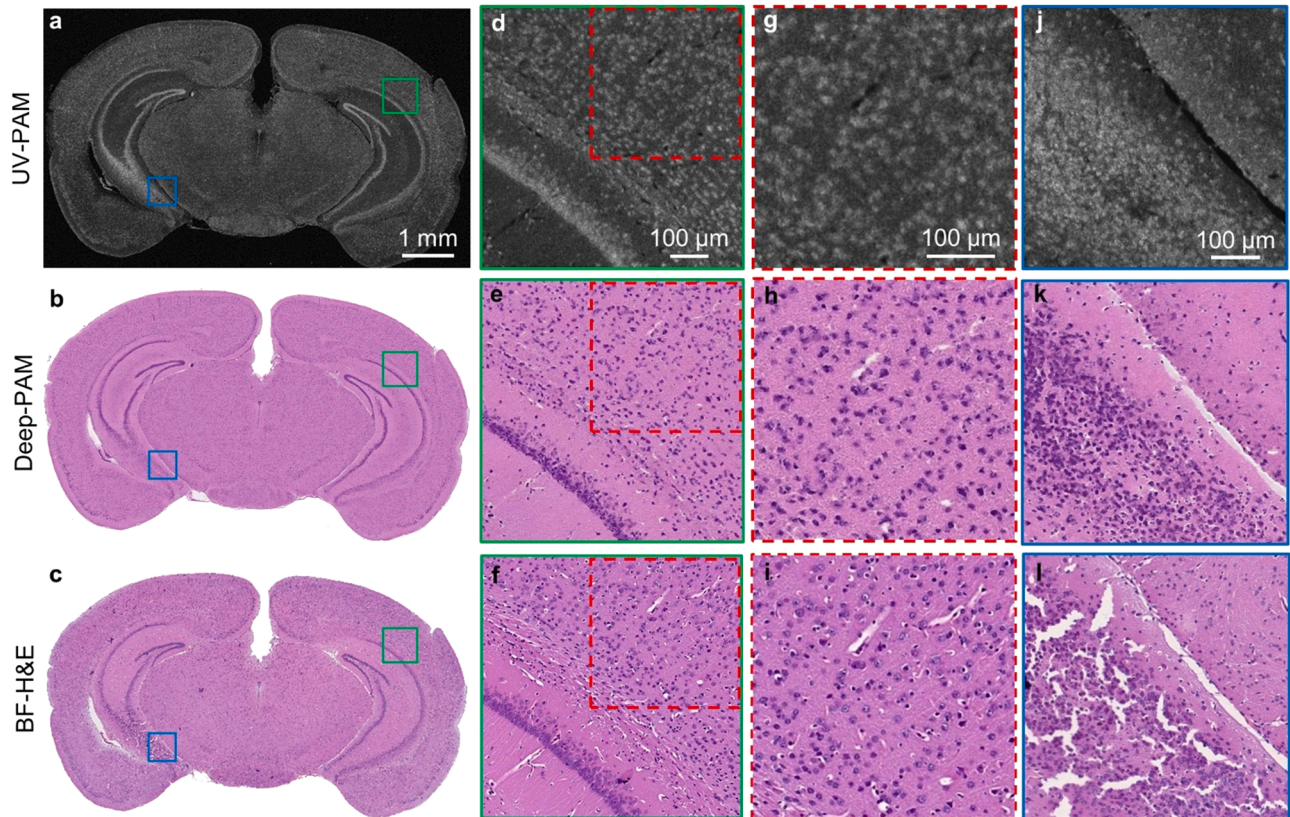


Fig. 4. UV-PAM and Deep-PAM validation using a 7- μm deparaffinized FFPE mouse brain section. a and b, UV-PAM and its corresponding Deep-PAM images of a 7- μm thick whole mouse brain section. c, The corresponding BF-H&E image of the same brain section after H&E staining, alcohol dehydration, and xylene clearing, serving as the ground truth for comparison. d-f, Zoomed-in UV-PAM, Deep-PAM, and BF-H&E images of the green regions in a-c, respectively. g-i, Zoomed-in UV-PAM, Deep-PAM, and BF-H&E images of the red dashed regions in d,e,f, respectively. The images are used for cellularity analysis. j-l, Zoomed-in UV-PAM, Deep-PAM, and BF-H&E images of the blue regions in a,b,c, respectively. Crumbling artifacts caused by xylene treatment in the clearing are shown in l. (For interpretation of the references to color in this figure legend, the reader is referred to the web version of this article.)

histological imaging method on thin FFPE brain sections. A 7- μm thick deparaffinized FFPE section was firstly imaged by the GM-UV-PAM system to acquire a UV-PAM image (Fig. 4a) and then stained by H&E to get the corresponding H&E-stained image (Fig. 4c) under a bright-field (BF) microscope. A pre-trained CycleGAN neural network transformed the UV-PAM image to a virtual H&E-stained image (i.e., Deep-PAM) (Fig. 4b), and the BF-H&E image (Fig. 4c) served as ground truth for comparison. According to the tissue absorption spectrum under the wavelength of 266 nm, the nucleus has high absorption, thus emitting strong PA signals, which explains the bright color of the nuclei in the UV-PAM image (Fig. 4a) or its zoomed-in images (Fig. 4d, g, and j). The gray color parts show the cytoplasm structures since the cytoplasm's absorption is relatively weak, leading to weak PA signals. Due to the positive contrast of the nucleus in the UV-PAM image, the cell morphology and distribution can be clearly observed. For example, the mouse brain's white hippocampus structure can be easily observed in Fig. 4a. For the BF-H&E image (Fig. 4c), the nuclei and cytoplasm are purple and pink, respectively. Obviously, the purple hippocampus structure has a high similarity with the white hippocampus structure in the UV-PAM image (Fig. 4a), with the difference in color and texture. The CycleGAN network has bridged the gap between these two sets of images by producing a Deep-PAM image (Fig. 4b) that provides almost the same textual and structural information as the corresponding BF-H&E image (Fig. 4c). It can be observed that the color and shape of the features in Fig. 4b and c are similar, which can be validated further by the zoomed-in green regions where individual cell nuclear can be distinguished (Fig. 4e and f) with high correspondence, which substantiates our deep-learning staining method's potency. We further zoomed in the red regions of Fig. 4e and f at a subcellular resolution for qualitative and quantitative cellularity analysis (Fig. 4h and i), which will be shown in Fig. 7.

Apart from providing almost the same information as the BF-H&E image, we also found that a Deep-PAM image can avoid some artifacts in

conventional BF-H&E image. It can be seen that a fair number of cracks appear in the BF-H&E image (Fig. 4l). As there is a high density of nuclei, a significant amount of information has been lost. However, in the Deep-PAM image (Fig. 4k), the section's morphology is intact, and there are no cracks artifacts. The crack artifacts are caused by the tissue clearing step in the H&E staining procedure. The need to better clear the tissue for BF imaging poses a threat of prolonged treatment of xylene, which leads to the generation of cracks in the tissue slice [34]. In contrast, as the tissue clearing step is not required in GM-UV-PAM imaging, both the UV-PAM and Deep-PAM images (Fig. 4j,k) of this region are intact.

In addition to histological imaging of FFPE sections, we applied our method to image frozen sections. Fig. 5a shows a UV-PAM image of a 7- μm thick frozen mouse brain section. Similar to the UV-PAM image of FFPE sections, the cells and cytoplasm are bright and gray, respectively. The trained neural network using FFPE sections can transform the UV-PAM image (Fig. 5a) to a virtual H&E-stained Deep-PAM image (Fig. 5b). Fig. 5c is the ground truth BF-H&E image for comparison. It can be observed that the BF-H&E image of frozen section (Fig. 5c) has significant artifacts and its quality is not comparable to the BF-H&E image of FFPE section (Fig. 4c). Despite the poor staining quality of the frozen section's BF-H&E image (Fig. 5c), the general structure of the tissue can still be recognized, such as the hippocampi (marked by the green solid boxes). However, the same hippocampi can be obviously observed in both the UV-PAM and virtually stained images (Fig. 5a and b), which are further zoomed in for comparison (Fig. 5d-f). Compared with the frozen section's BF-H&E image (Fig. 5f), the hippocampus and the individual cells surrounded the top of the hippocampus are clearer in the UV-PAM and its virtually stained Deep-PAM images (Fig. 5d and e) as they do not suffer from the poor staining. Another red regions in the brain cortex (marked in Fig. 5b and c) are also selected to show the superior performance of Deep-PAM over frozen section (Fig. 5h and i). However, it can be found that many nuclei are hollow in the BF-H&E image (Fig. 5i). This artifact is caused by ice crystals formed inside the

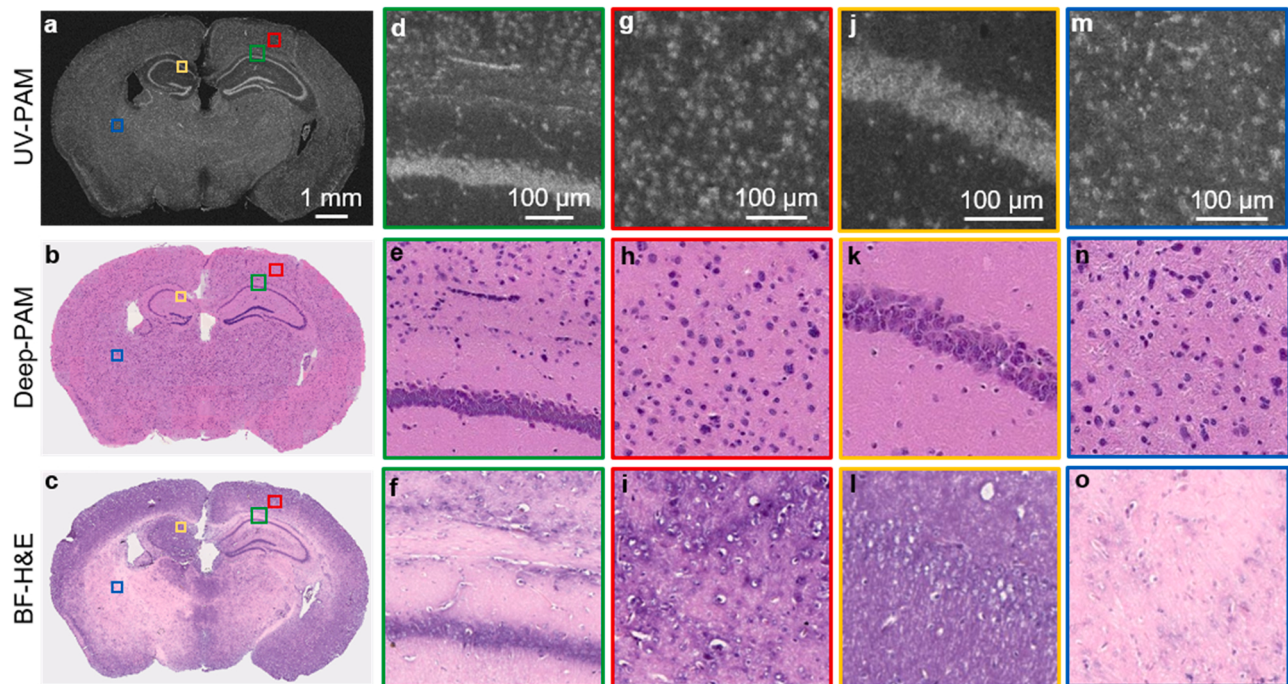


Fig. 5. UV-PAM and Deep-PAM validation using a 7- μm thick frozen section of a mouse brain. a–c, UV-PAM, Deep-PAM, and traditional H&E-stained image of a frozen sectioned slice. d–f, Zoomed-in UV-PAM, Deep-PAM, and BF-H&E images of the green regions in a–c, respectively, showing the ability of Deep-PAM to reveal individual cell nuclei. g–i, Zoomed-in UV-PAM, Deep-PAM, and BF-H&E images of the red regions in a–c, respectively, showing the ice crystal pitfalls. j–l, Zoomed-in UV-PAM, Deep-PAM, and BF-H&E images of the orange regions in a–c, respectively, showing the over-staining problem of hematoxylin in frozen section. m–o, Zoomed-in UV-PAM, Deep-PAM, and BF-H&E images of the blue regions in a–c, respectively, showing the under-staining problem of hematoxylin in frozen section. (For interpretation of the references to color in this figure legend, the reader is referred to the web version of this article.)

nucleus during tissue freezing, a typical pitfall of the frozen section approach [35]. In contrast, the UV-PAM image (Fig. 5g) and Deep-PAM image (Fig. 5h) still get an intact nuclear shape. Furthermore, Fig. 5j–l, m–o manifest the inconsistent H&E staining quality of the frozen section. The entire brain frozen section slice undertook the same staining process while some parts are over-stained, but others are under-stained. In Fig. 5l, the hippocampus is nearly not able to be distinguished due to the over-staining of hematoxylin, while in Fig. 5o, the individual nuclei are not obvious because of the under-staining of hematoxylin. However, this staining artifact will not appear in virtual staining images (Fig. 5k and n), as no staining chemicals are involved in our deep-learning staining method, which could unify the color tune and improve the diagnostic accuracy. It is obvious that our virtual staining method can not only successfully stain the frozen sectioned thin slice but also attain a better staining result than that of traditional staining.

The feasibility and reliability of Deep-PAM have been validated on both FFPE and frozen thin sections. We have further applied Deep-PAM to image a hand-cut and fresh brain tissue, with a thickness of around 2 mm. Fig. 6a and b are the UV-PAM and Deep-PAM images of the surface of the fresh brain specimen due to the limited penetration depth of UV excitation light. The imaged thick and fresh tissue was then

processed following the FFPE sample preparation protocol, and the top layer of the tissue surface is sectioned out for H&E staining and viewed under a microscope (Fig. 6c) to get an approximate ground truth histological image. The sectioned adjacent layer is slightly different from the surface layer imaged by UV-PAM due to the following two aspects: On the one hand, the fresh brain surface was warped once it is fixed in formalin during FFPE tissue processing. On the other hand, the sectioning process by a microtome may also lead to an orientation mismatch. However, it can be seen from Fig. 6b and c that the brain shows similar structures such as the cortex, corpus callosum, and caudoputamen. Note that the scale bars of Fig. 6b and c are different because of tissue shrinkage arising from the FFPE sample processing. The tissue can shrink around 60–70% after the FFPE processing [36]. The cortex regions next to the corpus callosum are zoomed-in, showing the performance of UV-PAM and Deep-PAM to reveal individual cell nuclei (Fig. 6d and e). A reference BF-H&E image (Fig. 6f) shows a similar cortex region in the adjacent layer. In addition, the cortex regions alongside the brain margin are also magnified for staining quality check (Fig. 6g–i). According to these zoomed-in cortex images, it can be noticed that the deep-learning staining can provide similar information as chemical staining even for thick and fresh tissue. Fig. 6j–l show the

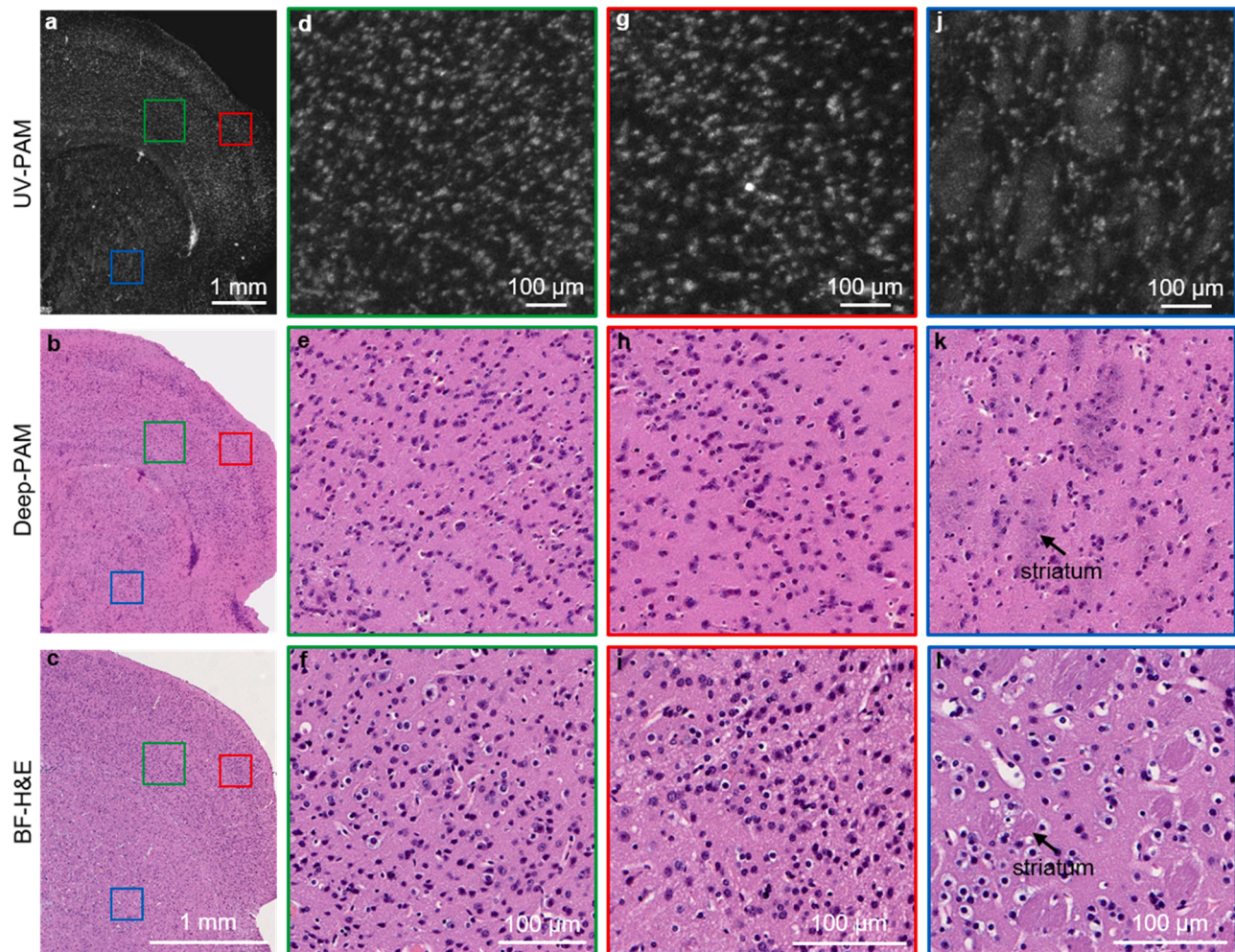


Fig. 6. UV-PAM and Deep-PAM validation by capturing the surface of a hand-cut 2-mm thick and fresh mouse brain. a and b, UV-PAM and Deep-PAM images of the thick and fresh mouse brain's surface. c, BF-H&E image of the layer next to the fresh mouse brain's surface for ground truth comparison. d and e, UV-PAM and Deep-PAM images of the cortex region (green regions in a and b) close to the corpus callosum in the fresh brain. f, BF-H&E image of the cortex region (green region in c) next to corpus callosum in the adjacent layer. g and h, UV-PAM and Deep-PAM images of the cortex region (red regions in a,b) in the fresh brain. i, BF-H&E image of the cortex region (red region in c) in the adjacent layer. j,k, UV-PAM and Deep-PAM images of the caudoputamen region (blue regions in a and b) in the fresh brain. l, BF-H&E image of the caudoputamen region (blue region in c) in the adjacent layer. (For interpretation of the references to color in this figure legend, the reader is referred to the web version of this article.)

related UV-PAM, Deep-PAM, and BF-H&E images of a region in the caudoputamen. The striatum structure can also be observed in our virtually stained image (Fig. 6k). To demonstrate the repeatability of the UV-PAM and its associated Deep-PAM for thick and fresh brain histological imaging, another fresh brain specimen with different brain structures (hippocampus) is imaged (shown in Supplementary Fig. S3).

Qualitatively, the UV-PAM image quality for FFPE or frozen section samples is similar, as indicated by Figs. 4a and 5a. However, the BF-H&E images are not highly consistent, where the BF-H&E image of the FFPE section (Fig. 4c) looks better than that of the frozen section (Fig. 5c) in terms of staining quality. FFPE-based sample preparation method provides more uniform and higher contrast histological images when compared with frozen section at the cost of long tissue processing time for sample processing and sectioning. Nevertheless, the quality of our Deep-PAM images is consistent for these two sample preparation protocols (Figs. 4b and 5b), which serves as a rapid imaging tool to provide stable and high-quality histological images for FFPE and frozen sections. The UV-PAM image quality of fresh tissue is better than FFPE section samples as there is no paraffin in fresh tissue affecting the UV-PAM imaging, leading to a better signal-to-noise ratio, thus improving the quality of Deep-PAM imaging of fresh tissue.

To evaluate the staining accuracy of our method, we first qualitatively visualize the similarity or distance among UV-PAM, Deep-PAM, and ground truth BF-H&E images of an FFPE section. The UV-PAM, Deep-PAM, and BF-H&E images (Fig. 4g-i) are cropped into small patches as three types of data points. The multidimensional scaling (MDS) algorithm is then implemented to visualize the similarity or distance among these three types of image data points (Fig. 7a). After the CycleGAN transformation, the UV-PAM images were turned into Deep-PAM images, with the resulting image data points closer to the BF-H&E images' data points. A further quantitative cellularity analysis about the number of cells (cell count) and their cross-sectional areas are made on the same Deep-PAM and BF-H&E images (Fig. 4h and i). The number of cells and average nuclear cross-sectional area are listed in Table 2. Besides, the cross-sectional area distributions are plotted in Fig. 7b.

Table 2 suggests that the number of cells from the Deep-PAM image is slightly lower than that of the ground truth BF-H&E image of FFPE sections and the average nuclear cross-sectional area of the Deep-PAM image is slightly larger than that of the BF-H&E image. The subtle differences for the cell counts and average nuclear cross-sectional area are believed to be mainly caused by the remaining paraffin that cannot be totally removed from the deparaffinized FFPE section. The residual paraffin will decrease the signal-to-noise ratio of the UV-PAM image,

Table 2

Counts (i.e., number of cells) and the average nuclear cross-sectional area of Deep-PAM and BF-H&E images (Fig. 4h and i).

	Counts	Average nuclear cross-sectional area (μm^2)
Deep-PAM	283	72.75
BF-H&E	289	70.66

lower the contrast of the nuclei, thus leading to a minor difference in the subsequent deep-learning histological staining. This imperfection will be minimized in fresh specimen imaging since no paraffin is used in fresh tissue.

4. Discussion

In contrast to the fluorescence-based histological imaging, our method totally relies on intrinsic biomolecular contrast, producing more consistent images. For example, in fluorescence imaging, various factors will affect the final imaging results, including the concentration of the dyes, the labeling time, micro-environments of tissue, and various tissue types. Moreover, GM-UV-PAM as a label-free imaging technique, we avoid the common photo-bleaching problem in fluorescence imaging. Compared with other label-free imaging modalities, such as SRS [22] and SLAM [26], which have been demonstrated to be able to generate histological images of un-sectioned fresh tissue, our GM-UV-PAM imaging system generates images with a higher speed [30]. Furthermore, our GM-UV-PAM imaging system is more cost-effective and compact, which only requires a solid-state laser with a size around $20 \times 10 \times 10 \text{ cm}^3$. The entire imaging system has the potential to be built on a small movable table that can be directly put inside an operating room, saving the turnaround time for intraoperative analysis.

As for the generation of virtually stained images, unlike the previous methods that applied a model-based mapping algorithm [22,37] to transform fluorescence or label-free images to virtual H&E-stained images pixel by pixel, which ignores the texture information [38], we adopted the emerging deep-learning methods that can produce high-quality virtually stained histological images together with the mapping of texture. Existing deep-learning-based transformation methods [4,5] have demonstrated their success in generating realistic histological images on thin microscopic sections. However, since these methods are supervised machine learning algorithms, which require input-output pairs, paired images are necessary for network training, involving complex image registration steps in data pre-processing. Hence, we employed an unsupervised learning method (CycleGAN) where unpaired data is already sufficient for network training. By

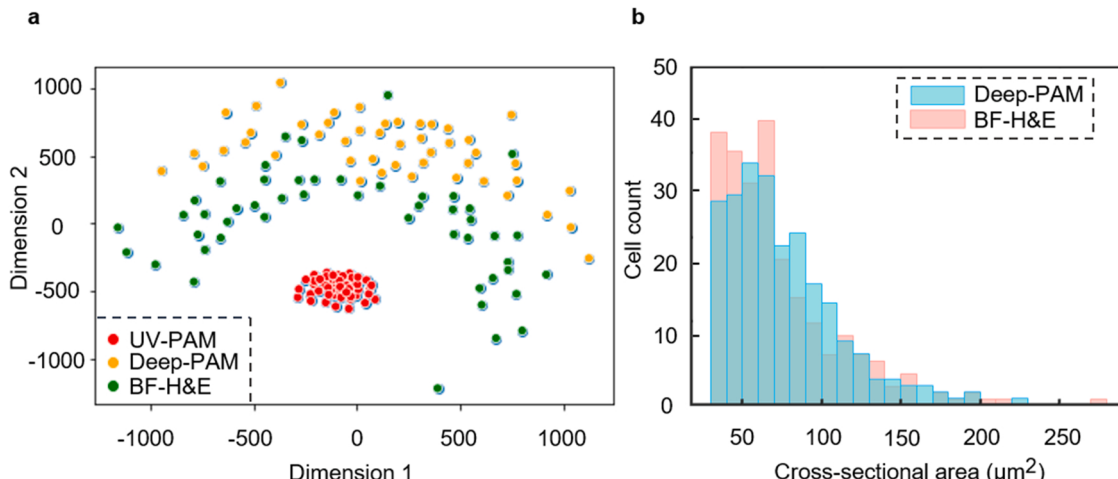


Fig. 7. Qualitative and quantitative analysis of Deep-PAM versus FFPE-based BF-H&E images from Fig. 4g-i. a, MDS plot showing the similarity or distance among UV-PAM, Deep-PAM, and ground truth BF-H&E images. b, Cross-sectional area distributions of the Deep-PAM and ground truth BF-H&E images.

utilizing CycleGAN, we achieved the high-quality style transformation between UV-PAM image and BF-H&E image using unpaired images, eliminating the need for the complicated image registration procedure. In addition, in the situations where paired data is not available, existing supervised methods cannot be trained, limiting its use in the staining of thick samples. However, CycleGAN can be directly trained with unpaired UV-PAM images of thick and fresh tissue and BF-H&E images of thin FFPE sections, achieving deep-learning virtual histological staining of thick samples (i.e., Deep-PAM images).

We demonstrated our Deep-PAM with H&E virtual staining because H&E staining is the most used staining method for pathological examination. Some other special stains, such as toluidine blue, a dye used by surgeons to highlight abnormal areas in premalignant lesions [39], can also be virtually stained with sufficient training data. The speed of Deep-PAM can be further improved by utilizing a UV pulse laser with a higher repetition rate. Furthermore, if the GM-UV-PAM system is implemented in a reflection mode, we can reduce the signal attenuation that the PA waves propagate through the thick tissue, further improving the signal-to-noise ratio and accommodating tissue with different thicknesses. In the future, by this virtual staining procedure, automated diagnosis implemented in many open-source whole slide imaging platforms can be integrated with transfer learning, further assisting pathologists for disease classification. With the intrinsic molecular imaging contrast, our Deep-PAM is expected to be applicable to various human organs, serving as a promising intraoperative and postoperative imaging tool for the medical community.

5. Conclusion

In this manuscript, by combining an unpaired image to image translation network (CycleGAN) with UV-PAM, we developed a high-speed histological imaging method that can not only get the virtual H&E-stained images of thin brain sections (both FFPE and frozen sections), but also be able to obtain virtual H&E-stained images of the surface of thick and fresh label-free specimens. This Deep-PAM imaging and virtual staining approach can be used in conventional histology to substitute the histochemical H&E staining process, thus saving time on human staining, bypassing chemical staining artifacts, or applied in the frozen section to get virtual histological images with high staining quality, eliminating the need to stain frozen sectioned slices. More importantly, it offers a new alternative for intraoperative analysis as it can acquire H&E histological images of a fresh tissue surface with a shorter time than that of frozen section (~ 20 min) [6]. To image a typical surface area of 5 mm × 5 mm for brain biopsy [40], the GM-UV-PAM takes less than 15 min [30], and the CycleGAN only needs ~ 10 s to transfer the captured UV-PAM image to its corresponding Deep-PAM image. Also, as the fresh tissue is directly imaged, no tissue processing and chemical staining is needed, saving lots of costs, such as the expenditure on the tissue processing machine, labor, and reagents. Simultaneously, the tissue shrinkage problem in traditional histology and freezing artifacts in the frozen section can also be avoided, probably providing more accurate information of the specimen. Finally, GM-UV-PAM imaging is a non-destructive process. Therefore, the imaged fresh tissue can be sent for conventional histology or other ancillary tests, preventing the need of harvesting additional tissue from patients for other testing.

Author contributions

L.K. and T.T.W.W. conceived of the study. L.K. and X.L. built the GM-UV-PAM imaging system and conducted the imaging experiments. L.K. and Y.Z. prepared the specimens involved in this study. L.K. processed and analyzed the data. L.K. and T.T.W.W. wrote the manuscript, which was approved by all authors. T.T.W.W. supervised the whole study.

Declaration of Competing Interest

T. T. W. W. has a financial interest in PhoMedics Limited, which, however, did not support this work. The authors declare no conflicts of interest.

Acknowledgements

The Translational and Advanced Bioimaging Laboratory (TAB-Lab) at HKUST acknowledges the support of the Hong Kong Innovation and Technology Commission (ITS/036/19); Research Grants Council of the Hong Kong Special Administrative Region (26203619); The Hong Kong University of Science and Technology startup grant (R9421).

Appendix A. Supporting information

Supplementary data associated with this article can be found in the online version at doi:10.1016/j.pacs.2021.100308.

References

- [1] T.S. Leeson, C.R. Leeson, *Charles R. Histology*, Saunders, 1970.
- [2] J. Rosai, Why microscopy will remain a cornerstone of surgical pathology, *Lab. Investig.* 87 (2007) 403–408, <https://doi.org/10.1038/labinvest.3700551>.
- [3] J. Yang, R.M. Caprioli, Matrix sublimation/recrystallization for imaging proteins by mass spectrometry at high spatial resolution, *Anal. Chem.* 83 (2011) 5728–5734.
- [4] Y. Rivenson, H. Wang, Z. Wei, K. de Haan, Y. Zhang, Y. Wu, H. Günaydin, J. E. Zuckerman, T. Chong, A.E. Sisk, L.M. Westbrook, W.D. Wallace, A. Ozcan, Virtual histological staining of unlabelled tissue-autofluorescence images via deep learning, *Nat. Biomed. Eng.* 3 (2019) 466–477.
- [5] Y. Rivenson, T. Liu, Z. Wei, Y. Zhang, K. de Haan, A. Ozcan, PhaseStain: the digital staining of label-free quantitative phase microscopy images using deep learning, *Light Sci. Appl.* 8 (2019) 1–11.
- [6] S.J. Maygarden, F.C. Detterbeck, W.K. Funkhouser, Bronchial margins in lung cancer resection specimens: utility of frozen section and gross evaluation, *Mod. Pathol.* 17 (2004) 1080–1086.
- [7] A.R. Pradipta, T. Tanei, K. Morimoto, K. Shimazu, S. Noguchi, K. Tanaka, Emerging technologies for real-time intraoperative margin assessment in future breast-conserving surgery, *Adv. Sci.* 7 (2020), 1901519.
- [8] T.P. Plesec, R.A. Prayson, C. Frozen, Frozen section discrepancy in the evaluation of central nervous system tumors, *Arch. Pathol. Lab. Med.* (2005).
- [9] J.B. Taxy, Frozen section and the surgical pathologist a point of view, *Arch. Pathol. Lab. Med.* 133 (2009) 1135–1138.
- [10] S.Z. Powell, Frozen section in the central nervous system, *Arch. Pathol. Lab. Med.* 129 (2005) 1635–1652.
- [11] J. Kang, I. Song, H. Kim, H. Kim, S. Lee, Y. Choi, H.J. Chang, D.K. Sohn, H. Yoo, Rapid tissue histology using multichannel confocal fluorescence microscopy with focus tracking, *Quant. Imaging Med. Surg.* 8 (2018) 884–893.
- [12] J. Dobbs, S. Krishnamurthy, M. Kyriish, A.P. Benveniste, W. Yang, R. Richards-Kortum, Confocal fluorescence microscopy for rapid evaluation of invasive tumor cellularity of inflammatory breast carcinoma core needle biopsies, *Breast Cancer Res. Treat.* 149 (2015) 303–310.
- [13] L.C. Cahill, J.G. Fujimoto, M.G. Giacomelli, T. Yoshitake, Y. Wu, D.I. Lin, H. Ye, O. M. Carrasco-Zevallos, A.A. Wagner, S. Rosen, Comparing histologic evaluation of prostate tissue using nonlinear microscopy and paraffin H&E: a pilot study, *Mod. Pathol.* 32 (2019) 1158–1167.
- [14] Y.K. Tao, D. Shen, Y. Sheikine, O.O. Ahsen, H.H. Wang, D.B. Schmolze, N. B. Johnson, J.S. Brooker, A.E. Cable, J.L. Connolly, J.G. Fujimoto, Assessment of breast pathologies using nonlinear microscopy, *Proc. Natl. Acad. Sci. USA* 111 (2014) 15304–15309.
- [15] K.N. Elfer, A.B. Sholl, M. Wang, D.B. Tulman, S.H. Mandava, B.R. Lee, J.Q. Brown, DRAQ5 and eosin (D&E) as an analog to hematoxylin and eosin for rapid fluorescence histology of fresh tissues, *PLoS One* 11 (2016), e0165530.
- [16] F. Fereidouni, Z.T. Harmany, M. Tian, A. Todd, J.A. Kintner, J.D. McPherson, A. D. Borowsky, J. Bishop, M. Lechpammer, S.G. Demos, R. Levenson, Microscopy with ultraviolet surface excitation for rapid slide-free histology, *Nat. Biomed. Eng.* 1 (2017) 957–966.
- [17] W. Xie, Y. Chen, Y. Wang, L. Wei, C. Yin, A.K. Glaser, M.E. Fauver, E.J. Seibel, S. M. Dintzis, J.C. Vaughan, N.P. Reder, J.T.C. Liu, Microscopy with ultraviolet surface excitation for wide-area pathology of breast surgical margins, *J. Biomed. Opt.* 24 (2019) 1.
- [18] A.K. Glaser, N.P. Reder, Y. Chen, E.F. McCarty, C. Yin, L. Wei, Y. Wang, L.D. True, J. Liu, Light-sheet microscopy for slide-free non-destructive pathology of large clinical specimens, *Nat. Biomed. Eng.* 1 (2017).
- [19] D.S. Gareau, Feasibility of digitally stained multimodal confocal mosaics to simulate histopathology, *J. Biomed. Opt.* 14 (2009), 034050.
- [20] P.K. Poola, M.I. Afzal, Y. Yoo, K.H. Kim, E. Chung, Light sheet microscopy for histopathology applications, *Biomed. Eng. Lett.* 9 (2019) 279–291.

- [21] R. Alford, et al., Toxicity of organic fluorophores used in molecular imaging: literature review, *Mol. Imaging* 8 (2009) 341–354.
- [22] D.A. Orringer, B. Pandian, Y.S. Niknafs, T.C. Hollon, J. Boyle, S. Lewis, M. Garrard, S.L. Hervey-Jumper, H.J.L. Garton, C.O. Maher, J.A. Heth, O. Sagher, D. A. Wilkinson, M. Snuderl, S. Venneti, S.H. Ramkissoon, K.A. McFadden, A. Fisher-Hubbard, A.P. Lieberman, T.D. Johnson, X.S. Xie, J.K. Trautman, C.W. Freudiger, S. Camelo-Piragua, Rapid intraoperative histology of unprocessed surgical specimens via fibre-laser-based stimulated Raman scattering microscopy, *Nat. Biomed. Eng.* 1 (2017) 0027.
- [23] C.H. Camp, M.T. Cicerone, Chemically sensitive bioimaging with coherent Raman scattering, *Nat. Photonics* 9 (2015) 295–305.
- [24] X. Chen, O. Nadiarynkha, S. Plotnikov, P.J. Campagnola, Second harmonic generation microscopy for quantitative analysis of collagen fibrillar structure, *Nat. Protoc.* 7 (2012) 654–669.
- [25] D. Débarre, W. Supatto, A.M. Pena, A. Fabre, T. Tordjmann, L. Combettes, M. C. Schanne-Klein, E. Beaurepaire, Imaging lipid bodies in cells and tissues using third-harmonic generation microscopy, *Nat. Methods* 3 (2006) 47–53.
- [26] S. You, H. Tu, E.J. Chaney, Y. Sun, Y. Zhao, A.J. Bower, Y.Z. Liu, M. Marjanovic, S. Sinha, Y. Pu, S.A. Boppart, Intravital imaging by simultaneous label-free autofluorescence-multiharmonic microscopy, *Nat. Commun.* 9 (2018) 2125.
- [27] Assayag, Large field, high resolution full-field optical coherence tomography: a pre-clinical study of human breast tissue and cancer assessment, *TCRT Express* (2013), <https://doi.org/10.7785/tcrtexpress.2013.600254>.
- [28] T. Wong, R. Zhang, P. Hai, C. Zhang, M.A. Pleitez, R.L. Aft, D.V. Novack, L. V. Wang, Fast label-free multilayered histology-like imaging of human breast cancer by photoacoustic microscopy, *Sci. Adv.* 3 (2017), e1602168.
- [29] D.-K. Yao, K. Maslov, K.K. Shung, Q. Zhou, L.V. Wang, In vivo label-free photoacoustic microscopy of cell nuclei by excitation of DNA and RNA, *Opt. Lett.* 35 (2010) 4139.
- [30] X. Li, L. Kang, Y. Zhang, T.T.W. Wong, High-speed label-free ultraviolet photoacoustic microscopy for histology-like imaging of unprocessed biological tissues, *Opt. Lett.* 45 (2020) 5401–5404.
- [31] J.Y. Zhu, T. Park, P. Isola, A.A. Efros, Unpaired image-to-image translation using cycle-consistent adversarial networks, in: Proceedings of the IEEE International Conference on Computer Vision, vols 2017–October, 2242–2251 (Institute of Electrical and Electronics Engineers Inc., 2017).
- [32] J. Johnson, A. Alahi, L. Fei-Fei, Perceptual losses for real-time style transfer and super-resolution, *Arxiv* (2016) 1–5.
- [33] Z. Wang, et al., Image quality assessment: from error visibility to structural similarity, *IEEE Trans. Image Proc.* 13 (2004) 600–612.
- [34] S.A. Taqi, S.A. Sami, L.B. Sami, S.A. Zaki, A review of artifacts in histopathology, *J. Oral Maxillofacial Pathol.* 22 (2018) 279.
- [35] Frozen Section Technique IV — Pathology Innovations. (<https://www.pathologyinnovations.com/frozen-section-technique-4>).
- [36] S. Chatterjee, Artefacts in histopathology, *J. Oral Maxillofacial Pathol.* 18 (2014) 111–116.
- [37] M.G. Giacomelli, L. Husvogt, H. Vardeh, B.E. Faulkner-jones, Virtual hematoxylin and eosin transillumination microscopy using Epi-fluorescence imaging, *PLoS One* 11 (2016) 1–13, <https://doi.org/10.1371/journal.pone.0159337>.
- [38] Y. Rivenson, K. De Haan, W.D. Wallace, A. Ozcan, Review article emerging advances to transform histopathology using virtual staining, *BMA Front.* 2020 (2020).
- [39] G. Sridharan, A.A. Shankar, Toluidine blue: a review of its chemistry and clinical utility, *J. Oral Maxillofacial Pathol.* 16 (2012) 251–255.
- [40] V. Leinonen, Assessment of β -amyloid in a frontal cortical brain biopsy specimen and by positron emission tomography with carbon 11-labeled pittsburgh compound B, *Arch. Neurol.* 65 (2008) 1304–1309.



Lei Kang received his bachelor's degree in Mechanical Engineering from Chongqing University. He received his master's degree in Bioengineering at the Hong Kong University of Science and Technology. He is currently a Ph.D. candidate in Bioengineering at the Hong Kong University of Science and Technology. His research areas center on applying different deep learning algorithms (image generation, image super resolution and object detection) in various medical imaging modalities.



Xiufeng Li is currently a Ph.D. candidate in Bioengineering at the Hong Kong University of Science and Technology (HKUST). He received his B.S. in Physics from South China University of Technology and M.S. in Bioengineering from HKUST. His research interests are in the design and development of practical photoacoustic imaging systems for clinical and pre-clinical applications.



Yan Zhang received her Master's degree in Optical Engineering from University of Chinese Academy of Sciences in 2018. She is currently a Ph.D. candidate in Bioengineering at Hong Kong University of Science and Technology. Her research areas focus on translational biomedical imaging and computational imaging.



Terence Tsz Wai Wong received his B.Eng. and M.Phil. degrees both from the University of Hong Kong, respectively. He studied in Biomedical Engineering at Washington University in St. Louis (WUSTL) and Medical Engineering at California Institute of Technology (Caltech), under the tutelage of Prof. Lihong V. Wang (member of National Academy of Engineering and Inventors) for his Ph.D. degree. Right after his Ph.D. graduation, he joined the Hong Kong University of Science and Technology (HKUST) as an Assistant Professor under the Department of Chemical and Biological Engineering (CBE). His research focuses on developing optical and photoacoustic devices to enable label-free and high-speed histology-like imaging, three-dimensional whole-organ imaging, and low-cost deep tissue imaging.